AIAA-94-0800
Effect of Initial Ice Roughness on Airfoil Aerodynamics

M. Bragg, M. Kerho and M. Cummings
University of Illinois at Urbana-Champaign
Urbana, IL

32nd Aerospace Sciences Meeting & Exhibit
January 10-13, 1994 / Reno, NV

THE EFFECT OF INITIAL ICE ROUGHNESS ON AIRFOIL AERODYNAMICS

M. B. Bragg*, M. F. Kerho+ and M. J. Cummings+
University of Illinois at Urbana-Champaign

ABSTRACT

Under most glaze icing conditions a smooth region in the vicinity of the stagnation point is followed by a rough region which forms at a well defined boundary. This smooth/rough boundary is believed to be due to increased heat transfer and the formation and freezing of water beads on the surface. It has been postulated that this may be due to boundary-layer transition occurring at this location. In order to study this phenomena, 1mm diameter hemispheres were placed on the leading edge of a NACA 0012 airfoil and the effect on the boundary layer studied at low subsonic speeds and Reynolds numbers from 750,000 to 2.25×10^6. Flow visualization and hot-wire anemometry were used to detect transition and determine the boundary-layer characteristics. The most forward location where a 0.5mm high roughness element caused transition was at x/c=0.015 at the lowest Reynolds number and at x/c=0.0075 at $Re=2.25 \times 10^6$. Standard methods to predict transition due to roughness based on a critical roughness Reynolds number consistently failed, predicting transition much closer to the stagnation point than that measured. It was postulated that these methods failed since most of the roughness elements were larger than the local boundary-layer thickness.

INTRODUCTION

The accurate prediction of glaze ice accretions on airfoils and other aircraft components is important to the design of aircraft which can operate safely in icing conditions. Glaze ice forms on the leading-edge in a shape that causes a significant loss in aerodynamic performance of the aircraft. Accurate a priori estimates of the loss in aircraft performance, stability and control can not be made if the shape of the glaze ice accretion can not be predicted with precision. Currently available ice accretion methods do not consistently provide this level of accuracy in the predicted shape of the ice accretion. Recent research suggests that this may be due to the simplistic assumptions made in the classic ice accretion model. The surface roughness appears to play a more fundamental role in the accretion process than once thought by coupling the flowfield, heat transfer and droplet impingement processes.

Ice accretion physics

The classic Messinger[1] model is based on a heat balance performed over a finite surface area and is the basis for current ice accretion models. This includes the surface roughness effects only through the heat transfer coefficient and in an averaged sense. Studies first by Olsen and Walker[2], and more recently by Hansman et. al.[3-5], have investigated the surface physics of the ice accretion process. These studies have revealed features quite different than the classic model particularly in the critical initial ice accretion phase.

Using close-up photography and videography Hansman[3-5] has studied the initial accretion of ice on cylinders. Three distinct surface roughness zones identifying different surface physics have been identified. A smooth zone near the stagnation point where a thin water film exists with no visible surface roughness. At some point downstream a significantly rougher zone exists where water beads are seen to form and freeze out. Here the ice accretion rate is significantly higher than in the smooth zone. The smooth/rough zone boundary is seen to move toward the stagnation point during the initial phase of ice accretion. At warm temperatures, a runback zone aft of the rough zone is observed. Water runs back on the surface into this region where it freezes as rivulets or as large coalesced water cells. In most cases horns originate from this region and are referred to as type B horns by Hansman[5].

The enhanced ice accretion rate in the rough zone is thought to be due to increased convective

* Associate Professor, Dept. of Aeronautical and Astronautical Engineering, Associate Fellow AIAA
+ Graduate Research Associate, Dept. of Aeronautical and Astronautical Engineering, member AIAA

heat transfer. Since a turbulent boundary layer is known to have much larger convective heat transfer at the surface, and surface roughness is known to promote boundary-layer transition, it has naturally been assumed by Hansman[4] that this smooth/rough zone interface is caused by boundary-layer transition. The movement of this boundary forward with time is somewhat more difficult to explain but recent infrared heat transfer measurements on roughness elements by Henry[6] and Hansman[5] reveal enhanced heat transfer on the element and up to 1/2 diameter ahead of each element.

Due to the harsh environment in the icing wind tunnel, and the difficulty in instrumenting an icing model, no studies of the detailed heat transfer or detailed flowfield have been conducted or are planned in an icing tunnel. Instead, the ice accretion and/or surface roughness must be simulated in a dry tunnel where the detailed measurements can be taken. Recently Shin[7] has studied the initial ice accretion on a NACA 0012 airfoil. Recognizing the importance of the smooth/rough zone boundary, he used close-up videography to quantify the surface roughness characteristics in this region. Closely packed hemispherical elements with heights from 0.28mm to 0.79mm were measured from the photographs.

The location of the zonal boundaries is thought to be important in determining the ultimate ice accretion shape. Particularly important is the behavior of the smooth/rough boundary as it indicates a significant increase in accretion rate. The behavior of the water film and beading, the state of the boundary layer and the heat transfer must be clearly understood before this process can be accurately modeled and used to improve ice accretion computer codes. This paper will focus on the physics of the boundary layer in this region. It will address the question of whether the smooth/rough zone boundary is indeed at the location of laminar to turbulent boundary-layer transition. Unfortunately, this type of boundary-layer transition is not well understood. What is known is reviewed in the next section.

Boundary-layer transition

For a smooth airfoil at low Mach number transition of the boundary layer usually occurs as a result of the development of Tollmein-Schlichting waves. These linear waves breakdown into nonlinear 3-D turbulent spots which merge to form a turbulent boundary layer. This process takes a finite distance to develop from the initial growth of the T-S waves to a fully developed turbulent boundary layer. Three-dimensional surface roughness causes transition due to a different mechanism and is therefore often referred to as bypass transition. The detailed flow physics of this process is discussed in more detail in the next chapter, here we focus on the empirical results derived from experiment.

Figure 1 shows a sketch of the flow when a laminar boundary layer encounters three-dimensional isolated roughness elements of different heights. It is useful to classify the elements based on their roughness Reynolds number, Re_k, where $Re_k = \rho U_k k / \mu$. Here U_k is the undisturbed velocity at height k, k is the roughness element height and μ and ρ are the air viscosity and density, respectively. The top element in Fig. 1 is too small to cause transition and the element wake trails downstream without growing. Here Re_k is small. In the flowfield some distance downstream of the second element the wake is seen to grow laterally resembling a wedge. The growth of the wedge indicates transition[8] and it is spreading laterally in the wedge at a half angle of 7-14 degrees[9] as the flow moves downstream. Here Re_k is larger than for the first element. The third element causes boundary-layer transition at the element itself, and the wedge extends from the element downstream. The height of the smallest element at this location which will cause transition at the element itself is k_{crit} and its Re_k is referred to as the critical value, $Re_{k,crit}$. For isolated 3-D roughness elements the value of $Re_{k,crit}$ is dependent on the shape of the roughness element[10,11] (i.e. sphere, hemisphere, cylinder, etc.) and varies from about 325 to 600. Hemispheres have been found to have a $Re_{k,crit}$ value from 325 - 450 depending on the experimental study[9,10].

Studies of the effect of distributed roughness on boundary-layer transition yield a $Re_{k,crit}$ = 600 independent of the shape of the roughness elements[12]. Boundary-layer stability theory on smooth surfaces shows that disturbances are damped in the stagnation region due to a favorable pressure gradient. It would therefore be anticipated that transition due to surface roughness might also be delayed by these stabilizing influences. Figure 2 (Ref. 12) shows the effect of Re_x, the Reynolds number based on surface distance from the stagnation point, on the critical Reynolds number, $Re_{k,crit}$. For Re_x > 150,000, $Re_{k,crit}$ is approximately 600. However, for Re_x < 150,000, $Re_{k,crit}$ increases with decreasing Re_x until a value of $Re_{k,crit}$ of approximately 1200 is reached near the leading edge. Braslow and Harris[12] and von Doenhoff and Horton[13] both measured this trend and speculated that it might be due to the favorable pressure gradient and stability near the stagnation point, and the fact that elements near the leading edge were protruding out of the boundary layer. The physics of how these factors effect transition are unknown.

Transition studies generally fall into 2 categories: 1) Applied studies to determine transition location for performance calculations, and 2) Basic studies into the physics of the instabilities and their growth which leads to transition. Little information on the details during the transitional process such as the surface convective heat transfer are available, particularly on rough surfaces. Recent measurements of transition location using surface hot-film sensors[14], which are actually heat transfer measurement devices, show surface velocity rms values much higher in the transitional region on smooth airfoils than in the turbulent boundary layer. This information is not available on rough surfaces, but if heat transfer peaks in the transitional region before the turbulent boundary layer is fully developed on rough surfaces, this could have a significant impact on the ice accretion process.

Summary

The location of the smooth/rough boundary during ice accretion and the enhanced heat transfer in the rough region are important features in the development of a better understanding of the physics of the ice accretion process. Boundary-layer transition at the smooth/rough boundary would help explain why heat transfer is increased and provide a framework on which to develop a model for the surface location where this boundary occurs. However, several fundamental aerodynamic questions must be answered before such a model can be formulated. First, and foremost, does boundary-layer transition (or the start of the transition process) really occur at this boundary? And if it does, how can the transition and therefore the smooth/rough boundary location be predicted based on the aerodynamic flowfield and roughness geometry? (How to predict the roughness geometry is also an important question but beyond our focus here.) What are the characteristics of the transitional region and how does the heat transfer behave in this region including the 3-D features on and around the roughness elements themselves?

This paper reports the initial results of an experimental study which, in cooperation with other experiments, hopes to answer these questions. In this paper, experimental results of the effect on the boundary layer of isolated 0.5mm hemispherical roughness elements on the leading edge of a NACA 0012 airfoil are reported. These roughness elements, depending on the Reynolds number and element location, are in a region of very favorable pressure gradient and often larger than the local boundary-layer thickness. Flow visualization and hot-wire boundary-layer measurements are used to study the effect of the roughness elements and results are examined in terms of the roughness Reynolds number, Re_k. Isolated elements were chosen for this initial study due to their ease of application and our better understanding of the transition mechanisms due to isolated roughness. Future experiments will use the same hemispherical roughness elements but in a distributed pattern modeling initial ice roughness.

EFFECT OF ROUGHNESS ON BOUNDARY-LAYER TRANSITION

This section reviews in more detail what is known about the effect of surface roughness on boundary-layer instability and transition. The focus is 3-D roughness geometries. The transition process on smooth surfaces has received much attention in the past few years and rather elaborate mathematical models have been developed with some success. Transition due to roughness has to this point defied detailed mathematical modeling, due in part to a lack of understanding of the important physical processes and the high degree of nonlinear interactions present in such a flowfield. Therefore, most of our limited understanding comes from careful experimentation on simple geometries. Since roughness induced transition may potentially play such an important role in the ice accretion process, it was felt useful to provide this brief review.

Smooth surfaces

For a smooth airfoil at low Mach number the path to transition usually begins with a linear growth of the "viscously tuned vorticity wave" known as a Tollmein-Schlichting(TS) wave[15]. As the amplitude of the TS waves grow, three-dimensional nonlinear interactions begin to occur and spanwise instabilities appear. Shortly after the appearance of these instabilities, continued nonlinear growth and interactions occur forming turbulent spots which later coalesce into fully developed turbulence. The introduction of surface roughness into the above processes can greatly enhance certain growth regimes or bypass others altogether.

There are three types of simulated roughness generally considered: a two-dimensional isolated roughness such as a spanwise 2-D trip, an isolated three-dimensional element such as a hemisphere or circular cylinder, and distributed roughness which can include grit and large numbers of densely packed hemispheres or cylinders. The effects of roughness are dependent upon its relative height in the boundary-layer. Usually roughness heights are nondimensionalized by the displacement thickness, k/δ^* or a roughness Reynolds number Re_k.

2-D roughness

Two-dimensional isolated roughness causes local areas of separated flow upstream and downstream of the element. The downstream separation can extend 40-50 roughness heights downstream before reattachment. Velocity profiles in this separated region have an inherent inflection point. This inflectional instability acts as a powerful amplifier for TS waves[16,17]. The road to turbulence is accelerated through the amplification of the primary TS instability by the inviscid Rayleigh mechanism. This powerful overamplification of a primary instability makes the 2-D trip the most efficient at causing early transition.

3-D isolated roughness

The means by which an isolated 3-D element affects the boundary-layer differs greatly from the 2-D isolated roughness discussed above. The qualitative effect of various shapes of elements, from hemispheres to circular cylinders, as determined from flow visualization experiments are fairly consistent. The critical roughness Reynolds number, $Re_{k,crit}$, or the Re_k where transition occurs at the element itself, are geometry dependent. Unfortunately, the values of Re_k and $Re_{k,crit}$ are also dependent on the experimental study from which they are derived. In this section, the Re_k and $Re_{k,crit}$ values are taken primarily from Morkovin[8] and are somewhat different from those in the Introduction which are from a variety of sources.

The qualitative 3-D topography of the locally separated flow around a 3-D element was first studied by Gregory and Walker[18] in 1956. A three view schematic of the flowfield topology for the "steady stage" of the flow about an isolated hemisphere is given in Fig. 3. Figure 3 represents the qualitative flowfield about the hemisphere for an $Re_k \approx 300$ or less, with no global pressure gradient along the wall. In this regime the flow about the element is stable and no turbulent wedge is formed downstream. From the side view of the element in Fig. 3(a) an incoming streamline comes to a stagnation point on the surface of the element. As fluid close to the wall approaches the element, an increasing pressure due to the presence of the element (adverse gradient) causes the incoming fluid to roll up into the primary vortex shown. Also present in the region in front of the primary vortex is a smaller secondary and tertiary vortex system. The primary vortex wraps around the element forming streamwise vortices which induce a downwash along the centerline of the wake. This vortex system is called the horseshoe vortex. A rear separation pocket is also formed in the near wake of the element. This separation pocket has "inlets" located at the bottom rear-quarters of the hemisphere below the horseshoe system. Other inflow to the separation pocket comes from the inner segments of the side and top stable shear layers. The "exit" or outflow from the separation pocket is a hole in the top rear shear layer in the form of two weak spiral vortices which move downstream and rotate in the opposite direction with respect to the horseshoe vortex[8]. Figures 3(b) and 3(c) show top and rear views giving an overall picture of the multiple vortex system. Currently, it is believed that all symmetric protuberances at low Reynolds numbers generate similar flowfields. These flowfields represent the stable base flow, and are the flowfields which would have to be perturbed in order to examine their stability analytically[8].

As Re_k is increased (350-450) the rear separation pocket begins to become unstable. As the separation pocket becomes unstable, the top shear layer also becomes unstable and begins to shed periodic hairpin vortices. Figure 4 shows a schematic of this hairpin structure. It is unclear at this point whether the sudden appearance of the hairpin structures is due to a strengthening of the weak spiral vortices weaving closer to the rear separation pocket as proposed by Morkovin[8], or by a completely separate mechanism. A recent study by Klebanoff et al.[10], proposes that the hairpin vortices are not the result of the spiral vortex filaments, but are an additional eddy shedding system that develops nonlinearly due to an inflectional instability in the mean velocity profile in the rear separation pocket. Klebanoff rationalizes that the "vagaries" of flow visualization might mask or not provide a clear picture of the unsteady processes which result in the production of the hairpin shedding system. The shedding frequency of the hairpin vortices is higher than that for a TS instability so that no TS amplification is induced into the surrounding boundary-layer. Detailed studies by Norman[19] found that these hairpin structures rise in the boundary-layer as they are convected downstream without introducing any new instabilities. As a result, transition occurs far downstream of the element generally due to a primary TS mechanism.

If Re_k reaches a critical value 400 to 600 depending upon the shape of the element, a local sudden onset of turbulence appears in the form of a turbulent wedge. The wedge first appears rather far downstream of the element. A slight increase in Re_k however, causes the wedge to move very rapidly upstream. The sudden appearance of the wedge *bypasses* the usual two-dimensional linear growth

of a primary instability. This type of transition is called bypass transition and was first coined by Morkovin in 1969.

If the element protrudes through the boundary-layer, Morkovin[8] and Norman[19] found that the secondary and tertiary horseshoe vortices upstream of the element, Fig. 3(a) become much larger and appear to play a more dominant role in the behavior of the flowfield. A spiral instability also forms on the primary horseshoe vortex. This larger system of horseshoe vortices represents the stable base flow for the protruding element. As Re_k increases in this system., the horseshoe vortices begin to oscillate. Continued increases in Re_k cause the oscillating horseshoe vortex system to collapse and reform periodically. This type of collapse and formation is called "burping." Ultimately, further increases in Re_k cause transition to occur in the horseshoe vortex system upstream of the element.

The effect of a favorable pressure gradient on isolated 3-D elements was studied by Peterson et al.[20] using spherical elements, and Bruin[21] who used cylindrical elements. Both researchers found little difference in their measured critical roughness Reynolds numbers when compared to similar experiments conducted in zero pressure gradient flows. For both studies the elements were contained completely within the boundary-layer.

Clearly the mechanism by which an isolated three-dimensional element induces transition in a boundary-layer differs greatly from the mechanisms observed for an isolated two-dimensional trip. The nonlinear growth mechanism and onset of the turbulent wedge eludes analytical explanation.

3-D distributed roughness

Although made up of the type of individual 3-D elements discussed above, the mechanisms by which distributed roughness effects a boundary-layer are to date unknown and only speculative. Studies involving distributed roughness have traditionally been conducted using densely packed grit where a nominal roughness height is usually determined from a profilimiter. For medium to large distributed roughness, no known instability mechanisms have been identified or documented. At Reynolds numbers below a critical Re_k, the boundary-layer appears to be unaffected by the presence of the distributed roughness. As $Re_{k,crit}$ is reached, nonlinear instability mechanisms transition the flow so rapidly that no differences are observed in the mean velocity profile. No inflectional velocity profiles are found, and no TS modes or amplifications have been observed. Transition due to distributed roughness truly bypasses the known routes to turbulence. Unlike 3-D isolated roughness, the shape of distributed roughness does not appear to be as critical in the determination of the Re_k at which transition occurs. For distributed roughness of a height less than the laminar boundary-layer thickness on a surface with no pressure gradient a fairly constant value of $Re_{k,crit} = 600$ is achieved.

Current speculations on the instability mechanisms are best summarized by Corke[17]. We know from the study of 3-D isolated protuberances that there exists a complex streamwise vortex system which emanates from an individual element. The impingement of this vortex system upon another element has a potentially destabilizing effect upon the vortex system of the downstream element. Due to the closeness of the elements, however, there might not be enough energy in the oncoming flow for downstream elements to generate their own regular vortex system. There will certainly be some sort of streamwise vortex interaction with possible amalgamation of smaller vortex structures. As the density of the elements increases, there are likely to be regions of dead fluid in the free space between elements. Much of this fluid is likely to have a very low velocity and consequently low inertia. As a result, this fluid will be highly susceptible to free-stream velocity and pressure disturbances. The above speculations on the instability mechanisms present in distributed roughness can be summarized as: 1) There should be some streamwise vorticity interaction with scales on the order of the roughness height k due to the element peaks and 2) The lower inertia fluid in the space between elements should be highly susceptible to free-stream and pressure disturbances.

The majority of recent research with distributed roughness has been conducted by Corke[17], Roshotko[22], and Morkovin[8] on a flat plate with zero pressure gradient. The above theories and speculations are the result of their work. Earlier studies by Braslow and Harris[12] and von Doenhoff and Horton[13] have produced some interesting results for distributed roughness effects on airfoils. The study by Braslow compiled data from several sources on the effect of the running Reynolds number based on the distance from the leading-edge, Re_x. Figure 2 is taken from Braslow's report and depicts the effect of Re_x on $Re_{k,crit}$. From Fig. 2, above an Re_x of approximately 150,000 the critical roughness Reynolds number is fairly constant at 600. Below 150,000, however, $Re_{k,crit}$ appears to increase linearly to 1200 as the leading-edge is approached. The experiment by von Doenhoff and Horton[13] studied the effect of distributed roughness in the leading-edge region of

a NACA 65(215)-114. A spanwise strip of grit was applied to the model at various locations near the leading-edge so as to effectively change the height of the roughness with respect to the laminar boundary-layer thickness. The chordwise extent of the roughness was 0.003 (grit strip width/chord). The tunnel speed was then varied until transition was observed at the roughness strip location. The lowest transition Reynolds numbers occur for the roughness contained completely within the boundary-layer thickness. As the element begins to protrude through the boundary-layer, the transition Reynolds number increases. As the element moves closer to the leading-edge and projects further outside the boundary-layer the transition Reynolds number increases substantially. This echoes the effect of Re_x on $Re_{k,crit}$ depicted in figure 2. The calculated $Re_{k,crit}$'s roughly match those shown in figure 2. von Doenhoff and Horton[13] hypothesized that the highly favorable pressure gradient might cause small eddies originating at the roughness peaks outside the boundary-layer to be damped out before they travel downstream far enough to cause instabilities to grow in the laminar layer. This effect has not been observed for isolated 3-D elements.

The effect of large distributed roughness in the stagnation region of an airfoil appears to be highly dependent upon the local Reynolds number based on surface length. The mechanisms by which the roughness elements induce transition, whether they are contained within the boundary-layer or protrude through, are to date unknown. The effect of a favorable pressure gradient on distributed leading-edge roughness is also unclear. It is not known whether the increase in $Re_{k,crit}$ is due to the favorable pressure gradient on the airfoil coupled with the slightly different flow physics of a protruding element, or a result of flowfield differences encountered in the stagnation region.

EXPERIMENTAL PROCEDURE

Model and Wind Tunnel

These tests were conducted in the subsonic wind tunnel at the University of Illinois at Urbana-Champaign. The tunnel is of conventional design with approximately a 3-by-4 ft test section. Test section speeds from zero to 160 miles per hour are available at Reynolds numbers of up to 1.5×10^6 per ft. The tunnel is of open return type and uses four turbulence screens and honeycomb in the settling chamber to reduce tunnel turbulence to below 0.1 percent.

The model used for this research is a 2-D model mounted vertically in the tunnel. The model had a span of 33.75 inches with a chord of 21 inches with a NACA 0012 airfoil section. The model is of a foam and fiberglass epoxy composite construction. Surface pressure taps were located in 2 chordwise rows, 7 inches above and below the model centerline. The roughness elements used were ruby hemispheres with a diameter of 1mm (and therefore a height above the surface of 0.5mm).

Flow Visualization

Flow visualization was performed using a fluorescent oil technique[23]. This technique allowed visualization of the laminar to turbulent transition front giving a good qualitative estimation of the location at which the boundary layer becomes fully turbulent.

A thin coat of heavy oil (10w-40) was first applied to the entire model surface under investigation. This coat of heavy oil was then toweled off. Mineral oil with a fluorescent additive was then sprayed onto the model surface in a very thin coat. The surface was illuminated using two 120 watt UV spotlights and two 4 foot UV fluorescent lamps causing the mineral to fluoresce in bright yellow. The base coat of heavy oil was reapplied after approximately five runs.

Tape was applied to the model seven inches above and below the model centerline. The tape was marked in 2% to 10% increments from leading edge to trailing edge to provide chordwise position to be determined from the photographs. The smaller increments were used for the regions of high surface curvature near the leading edge.

Each individual run was recorded using a Kodak Digital Camera System (DCS), 8mm Hi-8 video, and standard 35mm photography. For ease of data reduction purposes, the DCS was extensively used. The Kodak DCS uses a standard Nikon 35mm camera body that incorporates a Kodak CCD color imager. The imager records data on a 1280x1024 pixel matrix. The system provides high quality images over a wide range of exposures. Frames from the DCS were stored directly to a digital storage unit connected to a Macintosh computer. An ASA of 200 was used with exposure times from 0.5 to 1.0 seconds. DCS photographs were taken perpendicular to the chord line with the frame centered on the model centerline at the 50% chord location. Figure 5 shows a top view of the tunnel test section with the approximate camera position. Video was taken from the same camera location during the entire run until the oil pattern was established. Individual frames were then viewed

using Adobe Photoshop for online analysis and post run reduction. The turbulent wedges behind the roughness elements were digitized using Photoshop. The location where the roughness element wake began to grow into a wedge, which indicates the location of boundary-layer transition, was determined as well as the wedge angle.

Hot-Wire Anemometry

Boundary-layer mean and turbulent velocity measurements were obtained using a single hot-wire probe and an IFA 100 constant temperature anemometry system. The wires used were platinum coated tungsten with diameters of 4μm and 5μm. Due to the use of a single hot-wire probe, all measurements are the total velocity present at a given boundary-layer location. The boundary-layer velocity profiles were obtained by traversing the probe normal to the local surface using a 2-axis computer controlled traverse. The commercially available (VELMEX) traverse was used to position the probe with 0.01mm resolution. The traverse system was completely contained in a pressure sealed box adjacent to the test section with the hot-wire probe mounted on a support arm extending from the traverse, through the tunnel and into the test section, Fig. 5. Test section access was provided by a streamwise slot spanning the entire test section length.

Output from the IFA 100 system was lowpass filtered at 500Hz and acquired using a DT2801-A Data Translation A/D conversion board contained in a 386 type PC. Measurements were taken using a 1kHz sampling rate and 3500 samples were acquired at each boundary-layer location.

Probe velocity calibration was performed by moving the probe to a position approximately 6 inches in front of and 12 inches off the model surface. Calibration data were then acquired over a range of tunnel velocities from 0 to 155 mph. A least squares polynomial was then fit to the calibration data to obtain velocity as a function of hot-wire voltage. All hot-wire data were corrected for temperature and density variations from the calibration values. Turbulence intensity[24] was calculated from the velocity measurements using:

$$\text{Turbulence Intensity}(\%) = \frac{100}{U_\infty}\left[\frac{1}{T}\int_0^T u'^2\,dt\right]^{1/2}$$

Data Reduction and Error Analysis

Integral parameters calculated from individual velocity profiles include the boundary-layer momentum thickness θ, the displacement thickness δ*, and the shape factor H_{12}, and an integrated turbulence intensity. In order to calculate θ and δ* an edge velocity is required. The edge velocity was taken to be the maximum measured velocity for an individual profile. The equations for θ, δ* and H_{12} are given by[24]:

$$\delta^* = \int_0^\delta \left(1-\frac{u}{U_e}\right)dy, \quad \theta = \int_0^\delta \frac{u}{U_e}\left(1-\frac{u}{U_e}\right)dy, \quad H_{12} = \frac{\delta^*}{\theta}$$

Another helpful integral quantity is obtained by integrating the turbulence intensity from the wall to the edge of the boundary layer, in a similar manner as was done for the displacement and momentum thicknesses. This technique provides a measure of the amount of turbulent energy contained in a velocity profile. It is also helpful to normalize the integrated intensity values by δ. The equation used to calculate the normalized integrated turbulence intensity is given below:

$$\bar{\sigma}(\%) = \frac{100}{\delta}\int_0^\delta \left(\frac{u'_{rms}}{U_\infty}\right)dy$$

A source for error in these integral calculations can result from uncertainty in the probe distance from the surface. The alignment procedure used for these tests provided an uncertainty of ± 0.0025 inches in the location of the first boundary-layer measurement location normal to the model surface. The step size accuracy from this location was ± 0.0005 inches. Another source for error in the calculations is a heat transfer effect. As the hot-wire probe traverses close to the model surface (<0.3mm), heat is convected from the wire to the model surface. This increase in heat transfer from the wire is read by the anemometry system and calibration as a higher velocity than is actually present at the given measurement location. Due to the uncertainty in normal distance, no attempt was made to correct for the heat transfer effect at this time. This problem will be corrected in future measurements. During data reduction, points close to the surface which appeared to be affected were removed from the profile.

Critical Reynolds Number Calculations

Boundary-layer calculations for comparison to the measurements in this study and for use in the critical roughness height calculations were performed using the ISES computer code[25]. ISES is an airfoil aerodynamic analysis and design tool

which uses an iterative procedure between an outer inviscid solution and a viscous boundary-layer solver. The inviscid solution solves the Euler equations on an elliptic grid. The boundary layer is calculated using a two-equation lagged dissipation integral boundary-layer formulation and the Orr-Sommerfeld e^n criterion for determining transition. A value of n=9, which is the recommended value in ISES, was used.

To calculate critical roughness heights and values of Re_k, ISES is run and x/c, pressure coefficient C_p, the boundary-layer parameters displacement thickness δ^*/c, and momentum thickness θ/c are output to a file These values are input to a program which calculates critical roughness heights. The C_p is used to find the boundary-layer edge velocity. Displacement and momentum thickness values define the shape factor H_{12} which is used in the Karman-Pohlhausen 4th degree polynomial approximation to find the boundary-layer velocity profile. An iterative scheme is applied to determine critical roughness height based on a chosen critical roughness Reynolds number, $Re_{k,crit}$. Three cases of $Re_{k,crit}$ were chosen for the present analysis, $Re_{k,crit}$=375 for an isolated hemispherical element, $Re_{k,crit}$=600 as an upper bound for isolated elements and a typical value for distributed roughness, and $Re_{k,crit}$=a ramp from 600 to 1200 as given in Fig. 2 which attempts to include the additional stability found near the leading edge. The scheme found a roughness Reynolds number, $Re_k=\rho u_k k/\mu$ based on roughness height k and velocity at the top of the element u_k which was obtained from the Karman-Pohlhausen boundary-layer velocity profile. To determine the critical roughness height which just causes transition at the roughness element, the program iterated on k to obtain $Re_k = Re_{k,crit}$ as defined above for one of the three cases. When $Re_k = Re_{k,crit}$ the corresponding height is the critical roughness height k_{crit}.

RESULTS AND DISCUSSION

Results from the analysis of the flow visualization photos, hot-wire measurements and boundary-layer calculations are presented and discussed in this section. First results on the clean model are presented to demonstrate and validate the analysis methods for a well understood case. Then the results with the 0.5mm high hemispherical roughness elements on the leading edge of the airfoil are presented. Flow visualization and boundary-layer calculations were performed at 3 Reynolds numbers (0.75, 1.25 and 2.25 million), however, due to time constraints hot-wire data are only available for selected $Re=0.75x10^6$ cases.

Clean Model

Figure 6 shows the fluorescent oil flow visualization on the surface of the NACA 0012 airfoil at zero degrees angle of attack (α = 0 deg.) and Re = $0.75x10^6$. The photograph is oriented with the flow from right to left. Note the airfoil x/c locations are indicated in percent chord on the horizontal bands near the top and bottom of the photo. The oil flow responds to the shear stress on the model surface. Notice the relative lack of oil on the leading edge ahead of the 15 percent location and the large concentration between 15 and 30 percent. This is due to the high shear in the laminar boundary layer near the leading edge where the edge velocities are high and the boundary-layer profiles are still full. Several dark streaks are observed in the oil pattern, for example at 30 percent chord near the model centerline. This is the result of small dirt particles from the airstream becoming embedded in the oil. These are small and do not appear to affect the results. At about 72 percent chord, the oil from this location to the trailing edge has been scrubbed off and a dark surface appears in the photo. This corresponds to the boundary-layer transition location from laminar to turbulent flow.

Table 1 compares the transition locations at the 3 Reynolds numbers tested from the oil flow visualizations and the ISES airfoil analysis code. The comparisons are very good with the flow visualization results showing transition slightly ahead of the ISES predictions. Early transition on the model could be due to the tunnel turbulence level, model surface condition or the interpretation of the flow visualization. Since the difference between measurement and calculation increases with increasing Re, and shear increases with Re, the difference may be primarily a problem of interpreting the results. The transition is predicted in ISES using an e^n method which, for the shallow pressure gradient on the NACA 0012 airfoil at α = 0 deg., may be overly optimistic.

At a Reynolds number of 750,000 boundary-layer measurements were made on the clean model every 5 percent chord starting at x/c = 0.05. Figure 7 shows the velocity and turbulence intensity profiles at 4 chordwise locations. At x/c=0.25 a classic laminar boundary-layer velocity profile is seen. The corresponding turbulence intensity is 0.5 to 1%. At 65% chord the profile is still laminar with an increased boundary-layer thickness. However the turbulence intensity near the wall is beginning to grow indicating the start of the transition process. At 70%, just ahead of the 72% transition location indicated by the oil flow, the boundary-layer is well

into the transitional region. Notice that the velocity near the wall is larger at a given height from the wall as compared to the laminar profile, as is typical for turbulent boundary layers. The turbulence intensity has increased dramatically near the wall typical of what is sometimes referred to as peak transition[14]. At 80% chord a typical turbulent boundary layer profile is seen where the velocity increases rapidly next to the wall and more gradually and nonlinearly away from the wall. The turbulence intensity profile is typical of turbulent boundary layers with the shape and maximum value similar to that measured by Schubauer and Klebanoff[26] in their classic paper. Studying the velocity profiles, the velocity gradient at the wall and therefore the surface shear stress increases markedly at x/c = 0.70. Since the oil flow responds to surface shear, the oil is indicating a location near the start of the transition process and not a location after transition is complete. This may account for some of the discrepancy in Table 1.

These profiles can be integrated to obtain θ and δ^*. In Fig. 8 these boundary-layer parameters are plotted versus x/c for the clean airfoil at Re=750,000. These parameters are useful in determining the state of the boundary layer[24]. The displacement thickness, δ, indicates the inviscid thickness of the boundary layer and the momentum thickness, θ, is related to the total momentum removed from the stream by the boundary layer up to that location. δ and θ compare very well to the ISES results until the transition region is reached. The transition region is indicated by the drop in the value of δ^* as transition is initiated and the growth in δ^* indicates the fully developed turbulent boundary layer[24]. The measurements show that the transitional region begins at x/c=0.675 compared to 0.71 predicted by ISES. The transition region ends between x/c=0.75 and 0.80 based on the measurements and at 0.825 from the ISES prediction.

Overall the flow visualization results, hot-wire measurements and the ISES code compare well in terms of the transition location and boundary-layer development. The flow visualization shows transition slightly ahead of that predicted by ISES and this is supported by the hot-wire results. However the flow visualization may be indicating a slightly lower value of x/c at transition since it responses to the elevated surface shear seen early in the boundary layer during the transition process.

Roughness element results

The flow visualization and hot-wire results at Re = 750,000 are discussed first in this section and data are presented in Figs. 9-13. Figure 9 shows the flow visualization photos for all the elements and Re's tested, with the results summarized in Table 2. This section concludes by comparing the transition results as obtained from the flow visualization at all Re's to the empirical $Re_{k,crit}$ transition prediction schemes and is depicted in Fig. 14.

The flow visualization results for the Re=750,00 case with 0.5mm high hemispheres at 7 chordwise locations are shown in Fig. 9 a) and b). Elements located from x/c=0. to .0125 caused no transition wedges. The element at x/c=0.035 does generate a transition wedge and, although very faint, a wedge was also generated behind the x/c=0.015 hemisphere. Boundary-layer hot-wire measurements were made on the airfoil at Re=750,000 with roughness elements at x/c=0.0075, 0.015 and 0.035.

Figure 10 shows the boundary-layer shape factor H_{12} for the clean boundary layer and the boundary layer downstream of each of the 3 roughness elements. The measurements were conducted with only one roughness element on the airfoil at a time to avoid any interference. The clean airfoil H_{12} rises from a value of 2.6 at x/c=.20 to about 3.0 at x/c=.70. This corresponds to the laminar boundary layer region. H_{12} drops between x/c=.7 and .8 to a value of approximately 1.7. This is the transition region which is followed by the turbulent boundary layer. This corresponds to the data in Fig.8 since $H_{12}=\delta^*/\theta$. For the roughness element at x/c=0.0075 the values are different but the trends are very similar to the clean case. The H_{12} values initially are high compared to the clean values, but the value drops at x/c=0.6 and comes to a value of about 1.6 by x/c=0.75. Transition behind this element appears to be earlier, but by the same mechanism as the clean case. Morkovin[8] states that large roughness elements that do not cause bypass transition can contribute to a somewhat earlier growth of TS waves and secondary instabilities. That appears to be the case here where no bypass transition is seen (a turbulent wedge) but earlier TS transition is observed.

The behavior of the boundary layer downstream of the roughness elements at x/c=0.015 and 0.035 is quite different from the other case. H_{12} is decreasing from x/c=0.20 and on until a minimum value is reached far downstream. The element at x/c=0.035 starts at a lower H_{12} and reaches a minimum value sooner than the x/c=0.015 case. By 70 percent chord the H_{12} behind these two elements has reached values similar to the clean and x/c=0.0075 case. The low values of H_{12} suggest a significantly increased value of the momentum thickness. The momentum thickness development from the hot-wire measurements for these 4 cases is shown in Fig. 11. As suggested by the H_{12} values

the x/c=0.015 and 0.035 cases have significantly higher momentum thickness than the clean and x/c=0.0075 roughness element cases which both experience TS transition further back on the airfoil. These cases show an increase in the slope of θ versus x/c at the transition locations around x/c=0.60-0.70. No such behavior is seen in the x/c=0.015 and 0.035 cases. The x/c=0.035 element has a slightly higher θ value than the x/c=0.015 case over the first half of the airfoil. This indicates slightly higher momentum loss and therefore drag in the wake of the x/c=0.035 element. The x/c=0.035 case is the one which produces the most significant wedge development in the flow visualization photos.

So far the flowfield behind the hemispherical roughness elements at x/c=0.015 and 0.035 appear to be very similar in terms of the integral values based on the mean velocity profiles. However, the turbulence intensity in the 2 boundary layers are quite different. Figure 12 shows the integrated turbulence intensity, $\overline{\sigma}$, versus x/c for the clean case and the three roughness element cases. The clean boundary layer and the boundary layer behind the x/c=0.0075 roughness element are very similar with the roughness element causing slightly earlier transition as discussed before. The boundary layer behind the x/c=0.035 element has a gradually increasing integrated turbulence intensity which never exceeds a value of 3 percent. The flow behind the x/c=0.015 element has a rapidly increasing turbulence intensity which peaks at over 5 percent near x/c=0.35, then gradually drops with increasing x/c. This behavior is perhaps the opposite of what might have been expected since the x/c=0.035 element had a well defined wedge in the flow visualization whereas the x/c=0.015 case had only a very faint wedge. The reason these elements behave so differently may be due to their relative heights with respect to the local boundary-layer thickness. Table 2 or Fig. 14a) shows that the element at x/c=.015 extends up through the boundary layer into the inviscid stream, k/δ=1.25, while the x/c=0.035 element is completely submerged in the boundary layer with k/δ=0.89. The bypass transition mechanisms are different for the two cases[8] and this is probably reflected in the integrated turbulence intensity data.

Velocity and turbulence intensity profiles for the clean airfoil and airfoil with each of the roughness elements are compared at three x/c locations in Fig.13. At the x/c=0.20 location the velocity profiles for all cases reflect a laminar-type profile. At x/c=0.40 the velocity profiles for the x/c=0.015 and 0.035 cases are becoming more turbulent. Note that the x/c=0.035 case has a higher velocity near the wall than the x/c=0.015 case which explains why a well defined wedge is seen behind the x/c=0.035 element, Fig. 9a). By x/c=0.70 the x/c=0.0075 element case is showing a more turbulent profile than the clean case which corresponds to its earlier boundary-layer transition as seen before. The 2 roughness elements which promote bypass transition, x/c=0.015 and 0.035, have fully developed turbulent boundary layers are this point.

The turbulence intensity, σ, profiles also shown in Fig. 13 are more difficult to interpret. Two main features can easily be identified on each profile, the maximum value(s) of the turbulence intensity and its location(s) up normal to surface. Maximum values or spikes in the turbulence intensity appear at two different locations, 0.5mm off the surface and slightly less than 1.5mm off the surface. The clean case which is primarily T-S transition has both spikes, see also Fig. 7, x/c=.65. (Note that the lower spike height of 0.5mm, the same as the roughness element height, is probably a coincidence since it occurs for the clean case also.) The lower spike and upper spike merge in the transition region as shown at x/c=0.70 where peak values of σ are near 13%. Further downstream (not shown) the lower spike at 0.5mm off the surface is more dominant with a peak σ around 8%. The turbulence intensity in the boundary layer behind the x/c=0.0075 roughness behaves much the same as the clean case, however, the peak turbulence intensity values are always lower, even at x/c=0.90 (not shown). Turbulence intensity profiles behind the x/c=0.035 element are quite different from the clean and x/c=0.0075 element cases which experience TS transition. Behind the x/c=0.035 element the upper spike at 1.5mm above the surface never appears and only the lower spike is present. The lower spike reaches a max σ value of 5.5% and maintains this as it develops downstream merely adding more energy up off the surface in the thickening boundary layer. The turbulence intensity profile for the x/c=0.015 element which extends up beyond the edge of the boundary layer, has characteristics of both the clean boundary layer and that behind the x/c=0.035 element which is submerged in the boundary layer. Behind the x/c=0.015 element the double spike profile is seen, however the lower spike (see x/c=.40 profile) is better defined than in the clean case. The peak σ values are also quite large at about 10% but not quite as large as the clean case. Further downstream the x/c=0.015 σ profile takes a shape similar to the x/c=0.035 case.

What does all of this mean? Without more data (3 cases is not enough) and more analysis no definite conclusions can be drawn. However, some

clear trends can be identified which have been observed before[8] and are present in these data: 1) roughness elements which do not cause bypass, wedge-type transition can lead to earlier TS transition, 2) roughness elements large enough to cause transition, but submerged in the boundary layer, cause transition in a turbulent wedge by a different mechanism than TS transition, and 3) roughness elements which extend up out of the boundary layer cause transition in a wedge which is different than the first two mechanisms.

Transition prediction using $Re_{k,crit}$

Boundary-layer transition from roughness elements submerged and protruding through the boundary layer occur by different mechanisms. However, the empirical methods which use $Re_{k,crit}$ are based on the premise that the roughness is smaller than the local boundary layer thickness such that the velocity varies approximately linearly over the height of the element[13]. Only the method of Braslow and Harris[12] attempts a simple correction to $Re_{k,crit}$ to correct for their observed increase in k_{crit} near the leading edge stagnation point on an airfoil. In this section, the observed boundary-layer behavior behind the 0.5mm high hemispheres at 7 x/c locations and tested at 3 Reynolds numbers are compared to the $Re_{k,crit}$ based k_{crit} calculations to investigate how well these methods work for roughness elements typical of initial leading-edge ice accretions.

The flow visualization photos of Fig. 9 have been reduced as described earlier and the results are tabulated in Table 2 and plotted in Fig. 14. Since it is so difficult to determine precisely where the wedge starts to grow, only whether the wedge appeared at the element or downstream was indicated. In all cases measured, the fully developed wedges grew at an angle of approximately 12 degrees. In Fig. 14 several quantities are plotted in terms of height above the airfoil surface, y/c, versus distance along the surface from the stagnation point, s/c. First the boundary-layer thickness as predicted by ISES is plotted as the solid line. The critical roughness heights as calculated by the 3 methods are shown as dashed lines with different symbols to distinguish them. Finally, the hemispherical roughness elements themselves are plotted to scale which results in a half-ellipse shape due to the expanded y/c scale used. The roughness elements are coded with an open element being one that caused no early boundary-layer transition (no transition wedge), cross-hatched causing transition downstream of the element, and shaded elements caused transition at the element.

Examine first Fig. 14a) where the results for the Re=750,000 cases are shown. Note first that all the roughness elements except the one at s/c=0.049 (x/c=0.035) was taller than the local boundary-layer thickness. Remember the k_{crit} prediction methods using $Re_{k,crit}$=constant values assume that the element is completely submerged in the boundary layer. The k_{crit} predictions using constant values of $Re_{k,crit}$ of 375 and 600 do not work. The $Re_{k,crit}$=375 method predicts that all elements, except the one at the stagnation point (x/c=s/c=0.), will cause transition at the element. The $Re_{k,crit}$=600 method predicts that all elements except the first 2 will cause transition at the element. The flow visualization showed that no element caused transition at the element and only the last 2 elements at s/c=.026 and .049 (x/c=.015 and .035) caused transition downstream of the element. The method of Braslow which ramps from $Re_{k,crit}$=600 to 1200 as the leading edge is approached appears better. It predicts no transition at the elements for all the element locations tested.

At $Re=1.25x10^6$, Fig. 14b) all the elements extend up through the boundary layer. An unexpected result was observed where the roughness elements at s/c=.020 and .0235 (x/c=.01 and .0125) cause transition at the elements while the 2 elements downstream of these cause transition downstream of the elements. This is unexpected because the elements downstream have a higher Re_k than the upstream elements which caused transition at the elements. This may be a result of transition caused by different mechanisms since the downstream elements do not extend as far up out of the boundary layer as the elements further upstream toward the stagnation point. The $Re_{k,crit}$=375 and 600 methods, again do not work well, predicting transition due to elements which clearly do not cause transition wedges. The Braslow ramped method seems better, but the last element at s/c=.049 (x/c=0.035) has an Re_k=1335 well above the 600 required for transition at the element however, only transition downstream of the element is observed.

In Fig. 14c) all three k_{crit} methods predict that all the elements, except the one at the stagnation point (s/c=x/c=0.), will cause transition at the element. The observations from the flow visualization show that only the element at s/c=.02 (x/c=.01) and the 3 further downstream cause transition at the element. The element at s/c=.017 (x/c=.0075) caused transition downstream of the element. At $Re=2.25x10^6$ the boundary layer has become very thin and all the elements extend well up and out of the boundary layer. Note that the hemispherical element at s/c=0.013 (x/c=.005) does

not cause transition despite having an Re_k=1699, much larger than that required by any $Re_{k,crit}$ transition prediction method.

Shin[7] and Hansman[4] observed that the smooth/rough transition boundary at a given icing time moved forward as the chord Reynolds number of the body was increased. Here the same effect is seen with the elements closer to the leading edge causing transition as the Reynolds number was increased from 0.75 to 2.25 x 10^6. For example, consider the farthest forward roughness element that caused boundary-layer transition in a wedge either originating at the element or downstream. Converting the s/c values from Table 2 to mm (c=533.4mm), these locations are at s=14.1mm, 10.8mm and 9.1mm as Re increased from 0.75 to 2.25x10^6. Shin[7] recently tested a 21-inch chord NACA 0012 airfoil at zero degrees angle of attack in the NASA Lewis Icing Research Tunnel and observed the development of the initial ice roughness. At a slightly higher Re than the 2.25x10^6 tested here, under glaze icing conditions, a 7mm smooth zone width was observed afetr 1 minute of glaze ice accretion. The roughness in the smooth/rough boundary was approximately hemispherical with a height of 0.28mm (dia.=0.56mm). After 2 minutes the roughness height was 0.57mm (dia=1.11mm) with a boundary location 6mm back from the stagnation point. Adjusting for the slight increase in Re for Shin's[7] results, this agrees qualitatively with the location for the first transition wedge observed downstream of an element at Re=2.25x10^6 More data are required before this location can be confirmed to be the boundary-layer transition location. These data must include distributed roughness in addition to the single isolated roughness tested in this study.

SUMMARY

The effect of initial ice roughness on the leading-edge of a NACA 0012 airfoil was simulated using isolated hemispherical roughness elements. Hemispherical roughness elements 0.5mm high were placed at 7 locations from the stagnation point to x/c=0.035 and tested at Re = 0.75, 1.25 and 2.25x10^6. Surface flow visualization was used to detect boundary-layer transition due to the roughness and hot-wire boundary-layer velocity measurements were made for 4 Re=0.75x10^6 cases. The boundary-layer transition wedges due to the elements were compared to predictions from 3 different $Re_{k,crit}$ empirical roughness transition prediction schemes.

The measured boundary-layer transition location from the flow visualization compared well to the predictions from the ISES computer code on the clean airfoil. The hot-wire measurements of the boundary-layer velocity profile showed transition on the clean airfoil at Re=0.75x10^6. Changes in H_{12}, θ, δ^* and the integrated turbulence intensity mark the transition location.

Transition due to the hemispherical roughness could be seen in the oil flow visualization as turbulent wedges. The wedges appeared to grow in width at the location where boundary-layer transition first occurred in the wedge. The wedges when fully developed had a half angle of approximately 12 degrees. In no case did the roughness elements at the stagnation point or at x/c=0.005 cause transition. Hot-wire measurements downstream of 3 roughness elements at Re=0.75x10^6 revealed 3 different types of transition. The element at x/c=0.0075 did not form a wedge but contributed to early T-S transition. The element at x/c=0.035 was submerged in the boundary layer and formed a wedge downstream of the element. The momentum thickness was large compared to the clean case and the turbulence intensity was significantly less and its peak closer to the surface than the clean profile during transition and as a turbulent boundary layer. For the roughness element at x/c=0.015 the turbulence intensity was less than the clean case during transition but it showed the same double peak in maximum intensity. The velocity profile, however, more closely resembled the roughness cases at x/c=0.035.

Compared to the measured transition from the roughness elements, the $Re_{k,crit}$=375 and 600 based k_{crit} predictions always predicted transition much too far forward toward the stagnation point than was observed. The Braslow method which ramps $Re_{k,crit}$ from 600 to 1200 does better, but still over predicts transition significantly. In all cases the farthest forward element causing transition had a height larger than the local boundary-layer thickness.

Conclusions

Three major conclusions can be drawn from this study:

1) Transition due to an isolated roughness element occurs by a different mechanism if the roughness element is submerged versus those higher than the local boundary layer thickness. This has been reported previously in the literature and is supported by the measurements in this paper.

2) Based on this study it seems feasible that the *smooth/rough boundary during ice accretion* may be related to the boundary-layer transition location. However, this study used isolated roughness and actual ice has distributed roughness. A more detailed simulation of initial ice roughness must be tested before any serious conclusions can be drawn.

3) The empirical k_{crit} calculations based on $Re_{k,crit}$ values used to predict roughness induced boundary-layer transition are inadequate for the initial ice roughness case. For roughness near the leading edge which is much larger than the local boundary layer thickness, these methods predict transition too far forward.

Although it is still unclear if transition is at the smooth/rough ice accretion boundary, it is likely that boundary-layer transition is an important component of the physics of leading-edge ice accretion. If transition first occurs at the minimum k_{crit} value, and then moves forward due to water beads on the surface, transition may be the driver for determining the entire character of an ice shape under some glaze icing conditions. In other situations the transition location may occur further back on the accretion. The character of the transitional and turbulent boundary layer may still be important to the development of the ice accretion through the heat transfer. Regardless, accurate methods to predict boundary-layer transition due to large roughness will be needed for any improved ice accretion model. In addition, a better understanding of the heat transfer in the vicinity of roughness elements which do or do not cause transition is also needed.

ACKNOWLEDGMENTS

This research was supported in part by grant NAG 3-1134 from NASA Lewis Research Center. The digital camera system used to record the flow visualization was borrowed from NASA Lewis. The authors would also like to acknowledge the contributions of Dr. Jaiwon Shin and Dr. Mark Potapczuk of NASA Lewis and Dr. John Hansman of MIT. The authors have gained significantly in our understanding of the ice roughness problem through our many conversations with these individuals and others from the icing community.

REFERENCES

1. Messinger, B. L., "Equilibrium Temperature of an Unheated Icing Surface as a Function of Airspeed," *J. Aeronautical Sciences*, Vol. 20, No. 1, Jan. 1953.

2. Olsen, W. and Walker, E., "Experimental Evidence for Modifying the Current Physical Model for Ice Accretion on Aircraft Surfaces", NASA TM-87184, May 1986.

3. Hansman, R. J., Yamaguchi, K, Berkowitz, B., and Potapczuk, M., "Modeling of Surface Roughness Effects On Glaze Ice Accretion," AIAA Paper 89-0734, Jan. 1989.

4. Hansman, R. J., "Analysis of Surface Roughness Generation in Aircraft Ice Accretion," AIAA Paper 92-0298, Jan. 1992.

5. Hansman, R. J., "Microphysical Factors Which Influence Ice Accretion", *Proceedings of The First Bombardier International Workshop*," Montreal, Canada, Sept. 1993, pp. 86-103.

6. Henry, R. and Hansman, R. J., "Infrared Studies of Roughness Effect on Local Heat Transfer," *Proceedings of The First Bombardier International Workshop*," Montreal, Canada, Sept. 1993, pp. 382-384.

7. Shin, J., "Characteristics of Surface Roughness Associated with Leading Edge Ice Accretion," AIAA Paper 94-0799, Jan., 1994.

8. Morkovin, M. V., "Bypass Transition To *Turbulence and Research Desiderata*," NASA-CP-2386, May 1984, pp. 161-204.

9. Tani, I., "Effect of Two-Dimensional and Isolated Roughness on Laminar Flow," *Boundary Layer and Flow Control, Volume 2*," Ed. G. V. Lachmann, Pergaman Press, 1961, pp. 637-656.

10. Klebanoff, P. S., Cleveland, W. G., and Tidstrom, K. D., "On The Evolution Of A Turbulent Boundary-layer Induced By A Three-Dimensional Roughness Element.", *J. Fluid Mech*, Vol 237, 1992, pp. 101-187.

11. von Deonhoff, A. E. and Braslow, A. L., "The Effect of Distributed Surface Roughness on Laminar Flow," *Boundary Layer and Flow Control, Volume 2*," Ed. G. V. Lachmann, Pergaman Press, 1961, pp. 657-681.

12. Braslow, A. L. and Harris, R. V., "Use Of Grit-Type Boundary-Layer Transition Trips On Wind-Tunnel Models," NASA TN D-3579, Sept. 1966.

13. Von Doenhoff, A. E. and Horton, E. A., "A Low-Speed Experimental Investigation Of The Effect Of A Sandpaper Type Of Roughness On Boundary-Layer Transition," NACA Report 1349, 1956.

14. Nakayama, A., Stack, J. P., Lin, J. C. and Valarezo, W. O., "Surface Hot-Film Technique for Measurements of Transition, Separation, and Reattachment Points," AIAA Paper 93-2918, July, 1993.

15. Morkovin, M. V., "Panoramic View Of Changes In Vorticity Distribution In Transition Instabilities and Turbulence," FED-Vol. 114, Boundary-layer Stability and Transition to Turbulence, ASME 1991.

16. Morkovin, M. V., "On Roughness-Induced Transition: Facts, Views, and Speculations," *Instability and Transition, Vol. 1*, ed. M.Y. Hussaini and R.G. Voigt, , Springer-Verlag, New York, 1990, pp. 281-295.

17. Corke, T. C., Bar-Sever, A., and Morkovin, M. V., "Experiments On Transition Enhancement By Distributed Roughness," *Phys. Fluids*, Vol. 29, No. 10, October 1986, pp. 3199-3213.

18. Gregory, N. and Walker, W. S., "The Effects Of Transition Of Isolated Surface Excrescences In The Boundary-layer," British ARC, Res. Memo. 2779, 1956.

19. Norman, R. S., "On Obstacle Generated Secondary Flows In Laminar Boundary-layers and Transition To Turbulence," Ph.D. Thesis, Illinois Institute of Technology, 1972.

Table 1. Transition Location on the clean NACA 0012 Airfoil at α=0 deg.

	Transition location x/c(%)	
Re ($x10^{-6}$)	Flow visualization	ISES
0.75	72.	73.6
1.25	61.	65.3
2.25	49.	55.7

20. Peterson, J. B. and Horton, E. A., "An Investigation Of The Effect Of A Highly Favorable Pressure Gradient On Boundary-Layer Transition AS Caused By Various Types Of Roughness On A 10-Foot Diameter Hemisphere At Subsonic Speeds," NASA Memo 2-8-59L, April 1959.

21. Bruin, A. C., "The Effect Of A Single Cylindrical Roughness Element On Boundary-layer Transition In A Favorable Pressure Gradient," *Laminar-Turbulent Transition*, ed. D. Arnal and R. Michel, Springer-Velag, Berlin, 1990, pp. 645-655.

22. Roshotko, E., "Disturbances In A Laminar Boundary-layer Due To Distributed Surface Roughness," *Turbulence And Chaotic Phenomena In Fluids*, ed. T. Tatsumi, Elsevier Science Publishers B. V., North-Holland, 1984, pp. 39-46

23. Nguyen, V. D., Khalid, M. and Ellis, F. A., "On the Use of Less-Intrusive/Non-Intrusive Techniques for Detection of Boundary-Layer Transition in High and Low Speed Wind Tunnels at the Institute for Aerospace Research," *Proceedings of The First Bombardier International Workshop*," Montreal, Canada, Sept. 1993, pp. 317-345.

24. Schlichting, H., *Boundary-Layer Theory*, Sixth Edition, McGraw-Hill, New York, 1968.

25. Drela, M. and Giles, M., "A Users Guide to ISES", MIT Computational Aerospace Sciences Laboratory, Aug. 1989.

26. Schubauer G. B. and Klebanoff, P. S., "Contributions on the Mechanics of Boundary-Layer Transition," NACA TN 3489, Sept. 1955.

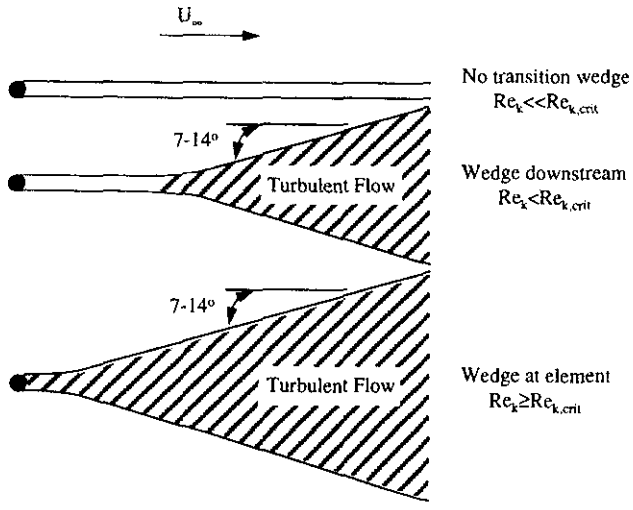

Fig. 1 Transition wedges due to 3-D isolated roughness

Table 2. Roughness Elements tested on the NACA 0012 Airfoil at α=0 deg.

$Re(x10^{-6})$	x/c	s/c	k(mm)	δ(mm)	Re_k	Transition wedge
0.75	0.	0.	0.5	0.	0.	none
0.75	0.005	0.0132	0.5	0.290	568.	none
0.75	0.0075	0.0170	0.5	0.316	634.	none
0.75	0.010	0.0203	0.5	0.349	670.	none
0.75	0.0125	0.0235	0.5	0.380	705.	none
0.75	0.0150	0.0265	0.5	0.399	723.	downstream
0.75	0.035	0.0488	0.5	0.560	798.	downstream
1.25	0.	0.	0.5	0.	0.	none
1.25	0.005	0.0132	0.5	0.224	946.	none
1.25	0.0075	0.0170	0.5	0.245	1057.	none
1.25	0.010	0.0203	0.5	0.269	1118.	at element
1.25	0.0125	0.0235	0.5	0.294	1177.	at element
1.25	0.0150	0.0265	0.5	0.308	1207.	downstream
1.25	0.035	0.0488	0.5	0.433	1335.	downstream
2.25	0.	0.	0.5	0.	0.	none
2.25	0.005	0.0132	0.5	0.166	1699.	none
2.25	0.0075	0.0170	0.5	0.181	1900.	downstream
2.25	0.010	0.0203	0.5	0.200	2011.	at element
2.25	0.0125	0.0235	0.5	0.217	2118.	at element
2.25	0.0150	0.0265	0.5	0.229	2173.	at element
2.25	0.035	0.0488	0.5	0.321	2405.	at element

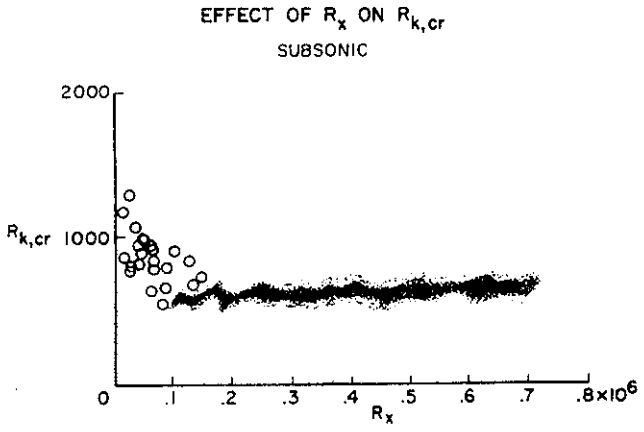

Fig. 2 Effect of R_x on $Re_{k,crit}$ for transition due to roughness (Braslow and Harris[12]).

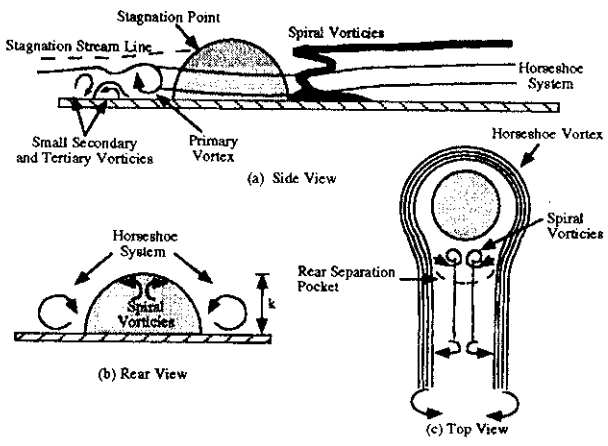

Fig. 3 Flowfield about a 3-D roughness during the steady state stage, $Re_k \approx 300$.

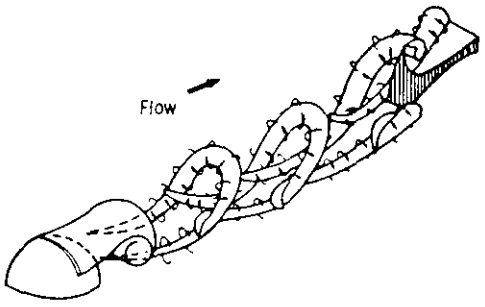

Fig. 4 Periodic hairpin vortex formation downstream of a hemispherical element[8].

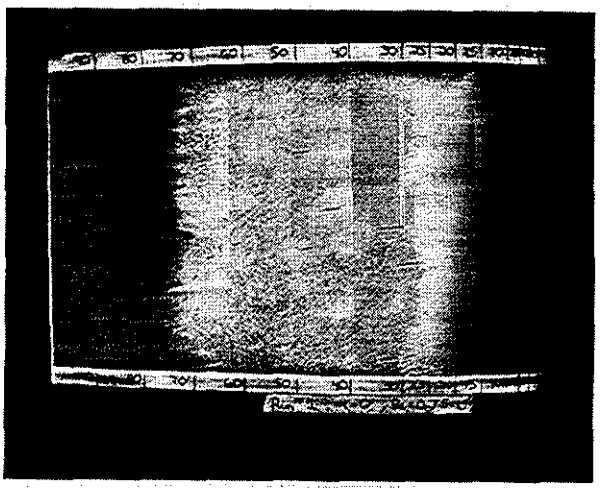

Fig. 6 Fluorescent oil flow on the NACA 0012 airfoil. (Re=.75x10^6, α=0 deg.)

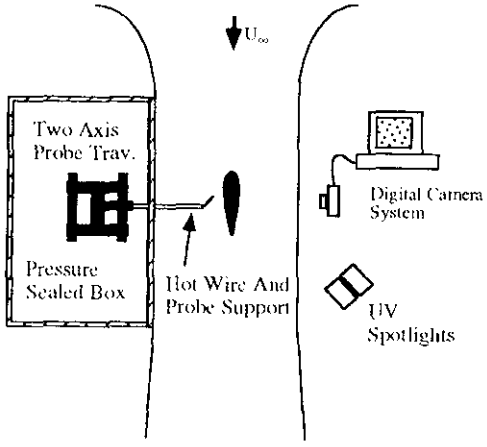

Fig. 5 Experimental set-up for hot-wire and flow visualization measurements.

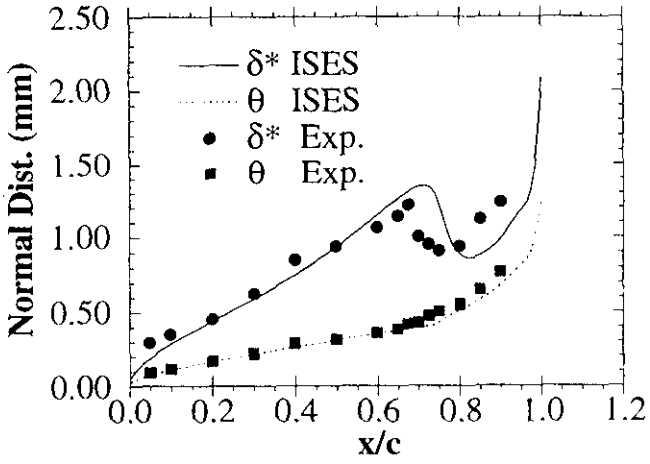

Fig. 8 Measured and calculated boundary-layer parameters on the NACA 0012 airfoil. (Re=.75x10^6, α=0 deg.)

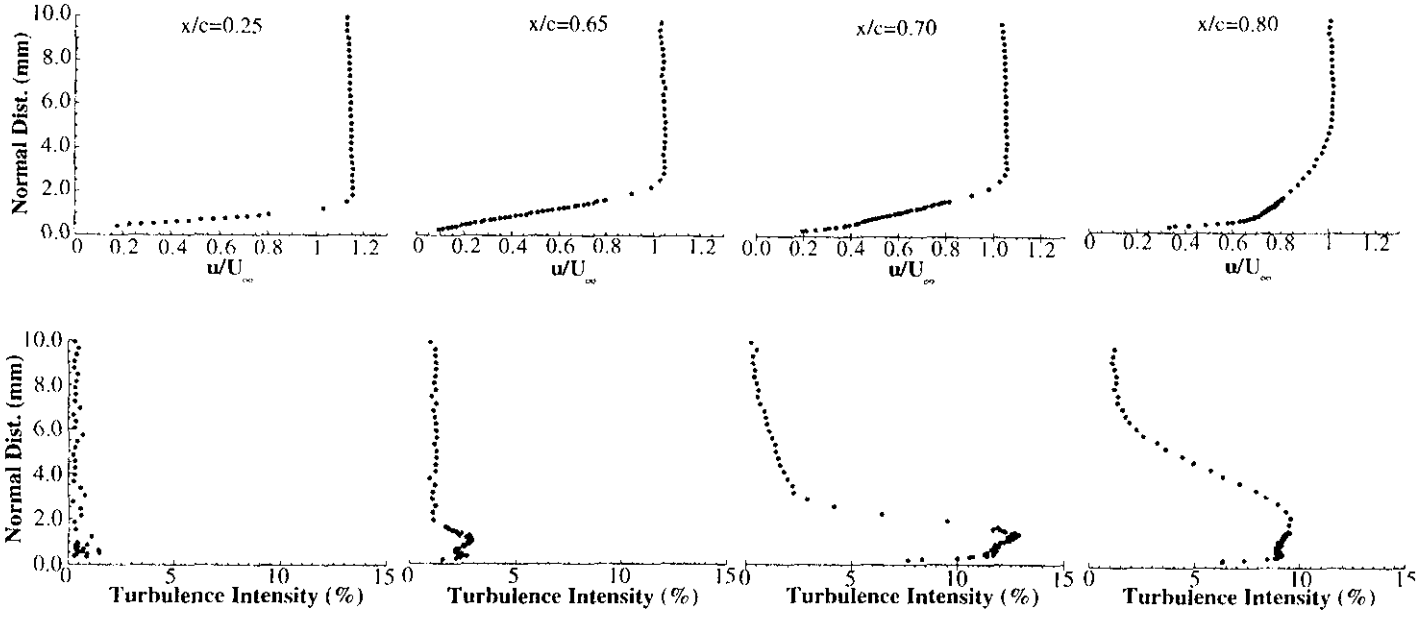

Fig. 7 Measured velocity and turbulence intensity profiles on the NACA 0012 airfoil. (Re=.75x10^6, α=0 deg.)

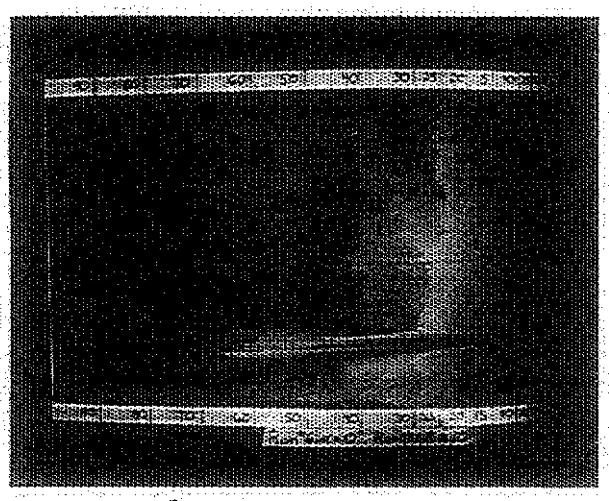

a) Re=0.75x10^6, roughness at x/c=0., .015 and .035.

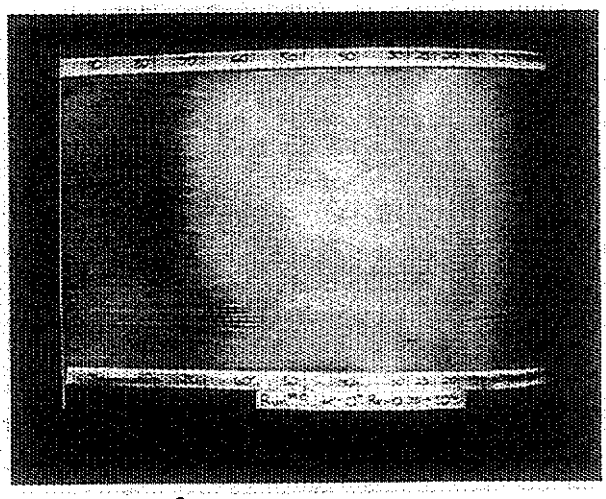

b) Re=0.75x10^6, roughness at x/c=.005, .0075, .01 and .0125.

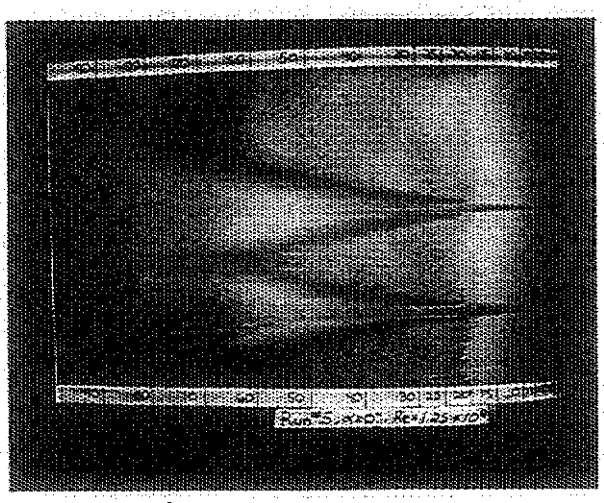

c) Re=1.25x10^6, roughness at x/c=0., .015 and .035.

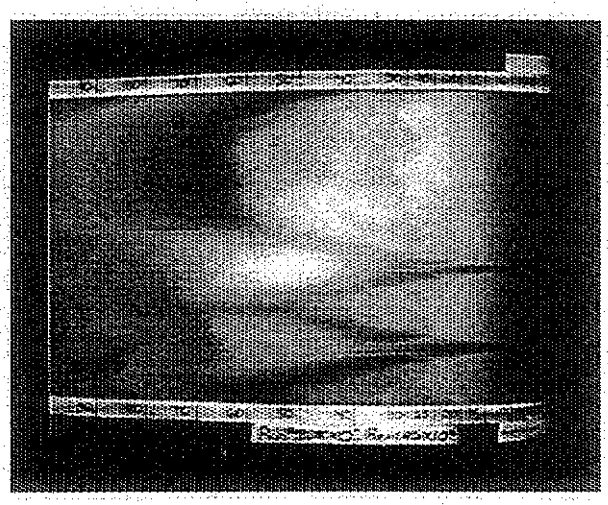

d) Re=1.25x10^6, roughness at x/c=.005, .0075, .01 and .0125.

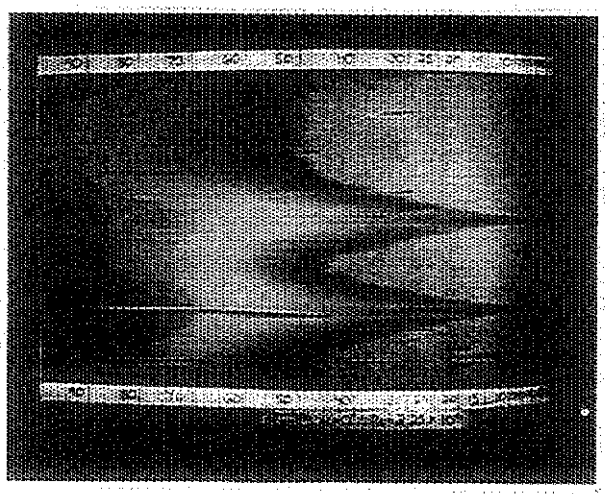

e) Re=2.25x10^6, roughness at x/c=0., .015 and .035.

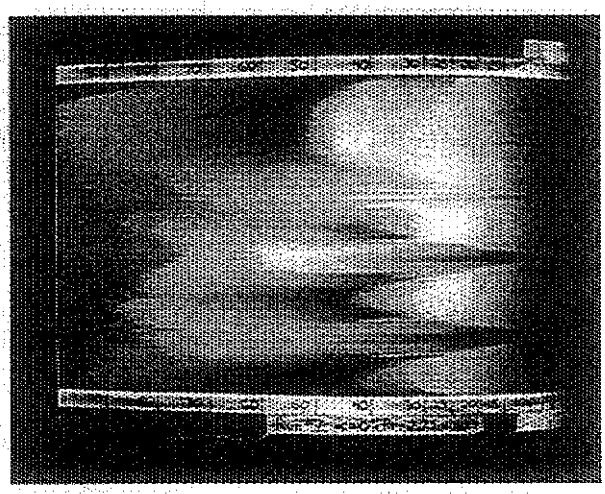

f) Re=2.25x10^6, roughness at x/c=.005, .0075, .01 and .0125.

Fig. 9 Surface oil flow visualization on the NACA 0012 airfoil with isolated 3-D, 1mm hemispherical roughness.

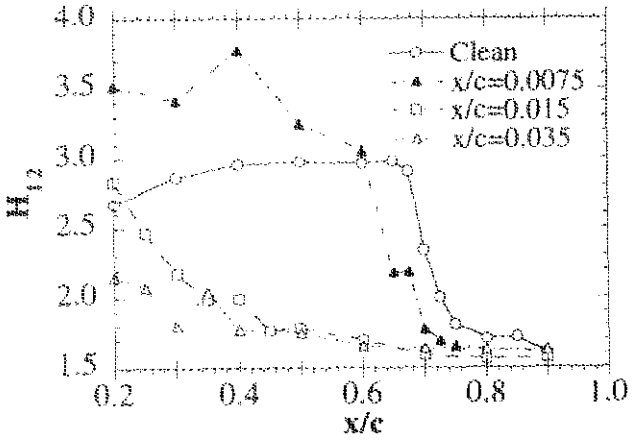

Fig. 10 Measured boundary-layer shape parameter clean and with roughness. (Re=0.75x10^6)

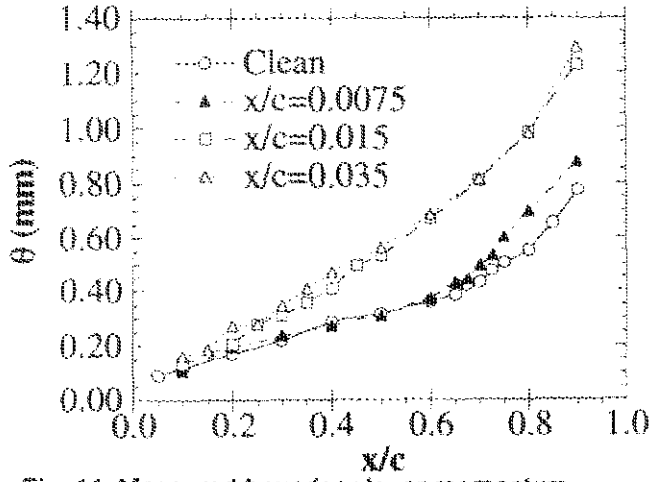

Fig. 11 Measured boundary-layer momentum thickness clean and rough. (Re=0.75x10^6)

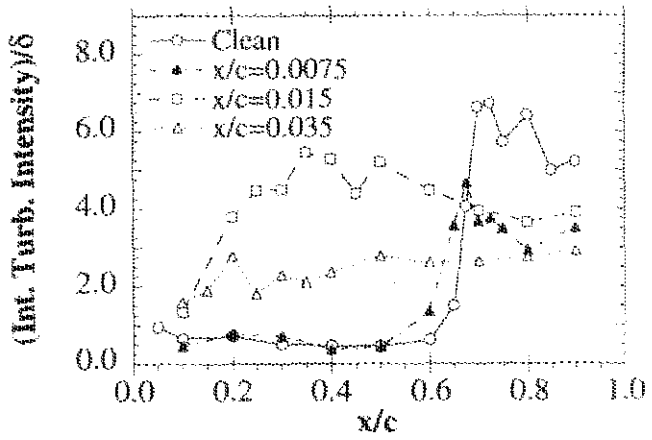

Fig. 12 Integrated turbulence intensity clean and with roughness. (Re=0.75x10^6)

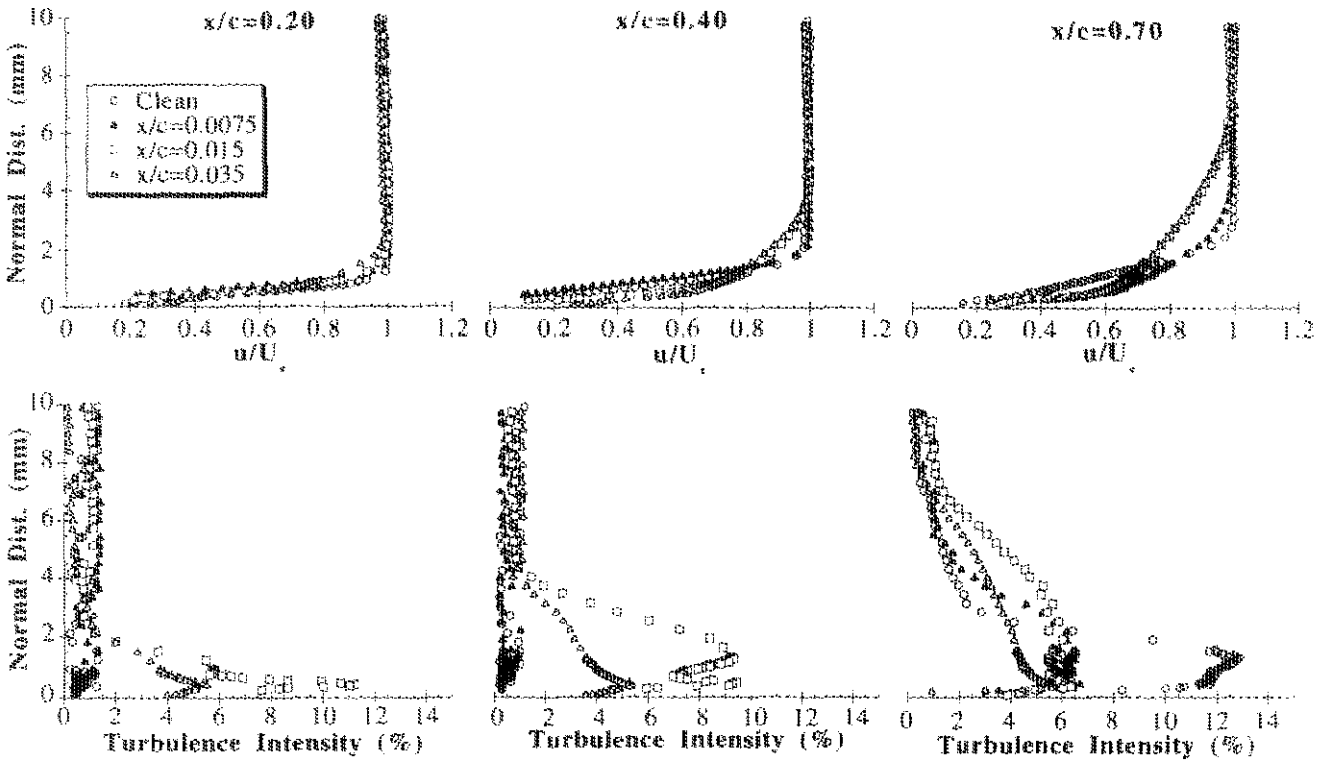

Fig. 13 Measured velocity and turbulence intensity profiles on the NACA 0012 airfoil clean and with roughness. (Re=.75x10^6, α=0 deg.)

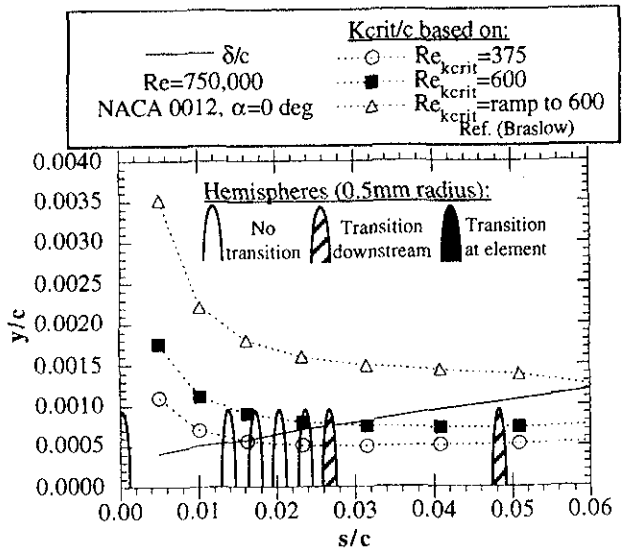

a) Re = 0.75x10^6

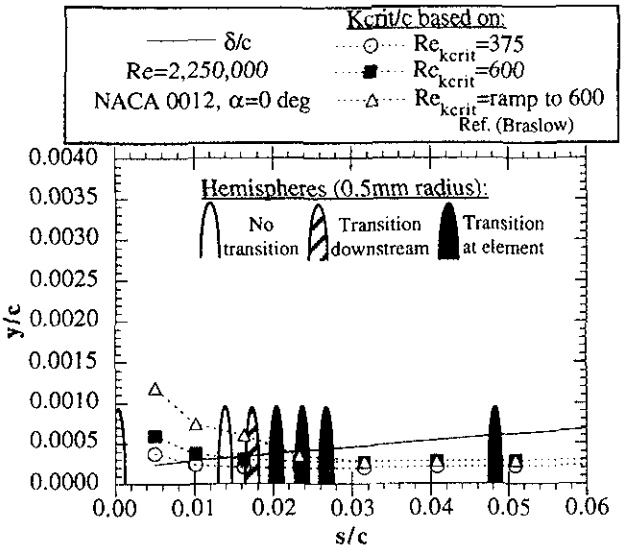

c) Re = 2.25x10^6

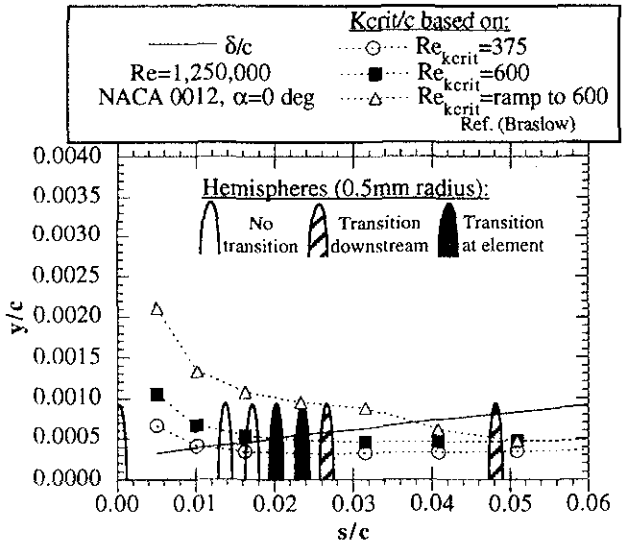

b) Re = 1.25x10^6

Fig. 14 Comparison of predicted critical roughness heights to experiment.